Mars Sample Return Return Trajectory and Thermal Protection System Design

Eric McNamara, Mohammad Ali Moghaddasi, Nate Thompson*
Cornell University, Ithaca, NY, 14853

The Mars Sample Return Earth re-entry thermal protection system and trajectory were designed to minimize the overall system mass and complexity. Trajectory design and preliminary thermal analyses were conducted in MATLAB to establish trends before more detailed (though one-dimensional) analyses were conducted with open-source industry packages. From the detailed analysis it was determined that a moderately steep initial entry trajectory and a 5 cm thick PICA heat shield ensure that the heat shield bond line remains adequately cool as to ensure mission safety.

I. Nomenclature

C_d	=	drag coefficient
h_w	=	wall enthalpy
h_0	=	free-stream enthalpy
$q"$	=	heat flux into heat shield
R	=	capsule nose radius
ρ_∞	=	free-stream density
V_∞	=	free-stream velocity
t_s	=	heat shield thickness
γ_0	=	initial vehicle flight-path angle at atmospheric interface
T_b	=	final bondline temperature

II. Introduction

The Mars Sample Return (MSR) mission is planned for returning geologic samples of Mars collected by the Perseverance rover to Earth in 2031. A European Space Agency (ESA) rover will pick up the samples left by Perseverance and will deliver them to a US-produced ascent module which will rendezvous with an ESA orbiter to fly the samples back to Earth, where finally a US-produced re-entry vehicle will deliver the samples to Earth's surface [1]. We aim to design the heat shield for this re-entry vehicle. Given the high re-entry velocity of the returning spacecraft on this trajectory, the design of the heat shield will be critical for mission success. To guide the sizing of the re-entry vehicle, and by extension its thermal protection system, we are using the mass and geometry of the re-entry vehicle on an early-2000's NASA trade study for a mission similar to the now-planned MSR mission [2]. That architecture consisted of a conical backshell with a maximum diameter of 1 m and a maximum mass of 50 kg. The re-entry vehicle's rough trajectory will be determined with the modeling outlined in Sections III.A and III.B, which will then be fed into the heating modeling outlined in Section III.C. This more detailed heating model using the Aerocapture Mission Analysis Tool (AMAT) will finally be used to generate the boundary conditions for a material response model in Porous material Analysis Toolbox based on Openfoam (PATO) to determine the optimal trajectory and thermal protection system thickness.

III. Trajectory Design

A. Mars–Earth Trajectory

We determined the transfer orbit between Earth and Mars that minimized the Δv at Mars, as the real Mars Sample Return orbiter and cruise stage would be aiming to minimize the Δv that it needs to provide. This means that the entry

---

*Undergraduate Students, Mechanical and Aerospace Engineering

speed at Earth is mostly a function of where Earth and Mars are in their orbits at this minimum Δv condition. A search for this trajectory was performed over the January 2030-January 2032 period, and the optimal trajectory was found to depart the Mars system on November 9, 2030 and arrive at the Earth system on July 11, 2031. The velocity at the edge of Earth's gravity well was found to be 5.65 km/s. The trajectories into the Earth's atmosphere were initially modeled with an ODE solver and assuming an exponential atmosphere. The initial conditions of the current simulations assume a spherical Earth and that the re-entry orbit is equatorial and prograde. Each trajectory within the Earth system is created such that the distance at the flyby periapsis in the case without an atmosphere is an input to the simulation. We found that for a capsule with the 2000's MSR's mass and cross-sectional area that the capsule will not re-enter if the initial periapsis is above ~45 km, but this is refined in the detailed analysis in Section III.C.

B. Earth-Entry Trajectory First Analysis

Initially, we modeled the heat transfer into the heat shield using the correlation proposed in eq. 6.169 of Anderson [3]: $q'' = \rho_\infty^N V_\infty^M C$. For the stagnation point, Anderson proposes $M = 3$, $N = 0.5$, and $C = 1.83 \times 10^{-8} R^{-1/2}(1 - h_w/h_0)$, where ρ_∞ is the free stream density, V_∞ is the free stream velocity, R is the nose radius, and h_w & h_0 are the wall and total enthalpies. To assume a worst case scenario, we took h_w/h_0 to be zero, but in the material response modeling below, this assumption is relaxed.
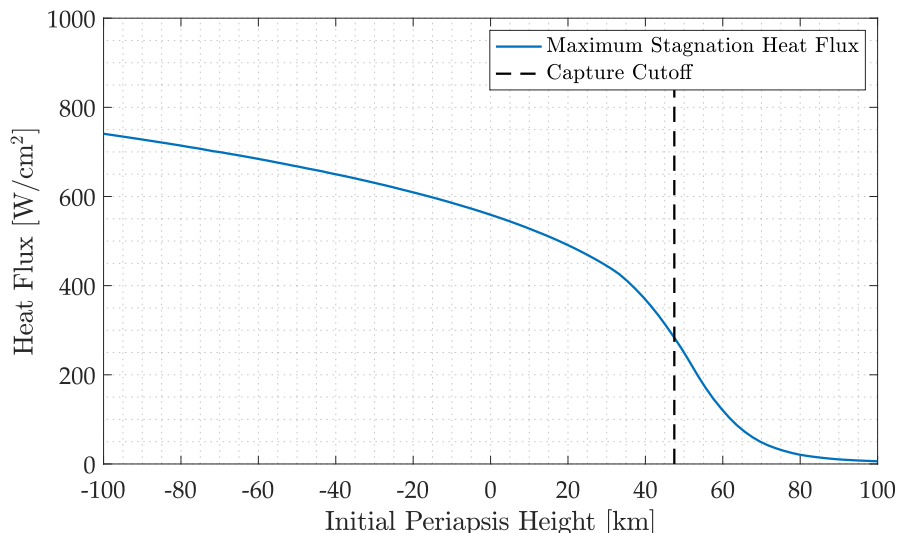

Fig. 1   Preliminary analysis of peak heating experienced at the stagnation point, as outlined in Sections III.A and III.B

Our preliminary findings, again based on the 2000 MSR concept, show a peak heating highly dependent on our initial periapsis: with periapsis nearly high enough to not capture, peak heating is about 400 W/cm^2 and only increases with decreasing initial periapsis height. For comparison, the peak heating for the Stardust mission was upwards of 1000 W/cm^2 [4, 5]. The predicted heating is shown in Figure 1, and shows that the maximum heat flux into the heat shield is minimized with the highest possible incoming periapsis. Conversely, Figure 2 demonstrates that for shallower entries the total heat load absorbed by the heat shield is significantly higher than at steeper entry angles. The mechanisms for the inverse behavior are discussed in detail in Section III.C. Regardless of the underlying mechanism, this behavior implies there will be a trade-off to be made in the detailed design, and as such three trajectories with varying incoming periapses are discussed in the detailed modeling stages below.

C. Earth-Entry Trajectory Detailed Analysis

1. Analysis Setup

We analyzed the performance of our heat shield design at three different flight-path angles: -90°, -10.96°, and -6°. The flight-path angle of -90° is an extreme case, and it corresponds to an initial periapsis at the center of the earth. The
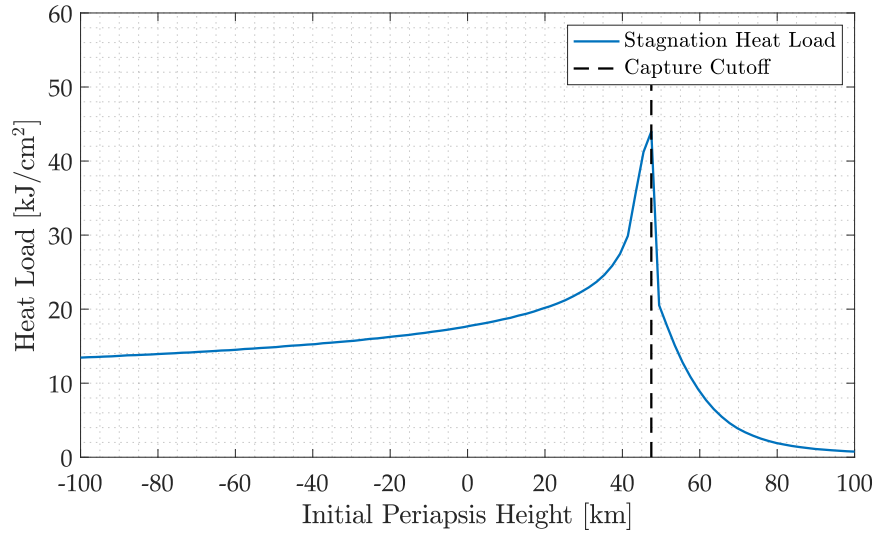
Fig. 2   Preliminary analysis of the total heat load experienced at the stagnation point, as outlined in Sections III.A and III.B

angle of -10.96° is associated with an initial periapsis of 100 km below mean sea level, and the angle of -6° is associated with initial periapsis at 36.3 km above mean sea level.

Before running AMAT, there are a number of important parameters that need to be defined. The angle of attack of the re-entry vehicle is set to zero as it is not implemented in the AMAT source code, and the initial longitude, latitude, and heading were set to zero since they would not have a significant impact on the analysis. Note that this corresponds to re-entering over the equator in the prograde direction. The lift-to-drag ratio of the blunt-body capsule is effectively zero as it experiences substantially more drag than lift, and the bank angle was set to zero as it was assumed that the capsule would have an axisymmetric mass distribution.

For the nonzero parameters, we need to define the mass, aerodynamic area, ballistic coefficient, initial height, initial velocity, flight-path angle, propagation time, and nose radius. In the early 2000's NASA conducted a trade study for a mission that was similar to our Mars Sample Return mission. This paper from the JPL outlined significant details about the Spacecraft Systems Architecture for Mars Sample Return mission, including for the re-entry phase. We use the mass and geometry of this vehicle, and so the mass of our re-entry vehicle is 50 kg [2]. The vehicle has a circular cross-section with a diameter of 1 meter at its widest point. Since the vehicle's angle of attack is 0°, the aerodynamic area was simply the area of the maximal cross-section, i.e. $\pi/4(1 \text{ m})^2 = 0.25 \text{ m}^2$. We also assume the same general form factor as the stardust mission, so we use a nose radius of 0.228 meters. To find the ballistic coefficient, we first need to determine the drag coefficient. From a paper that investigated the aerodynamics of ducted re-entry vehicles, the authors use a baseline geometry that was representative of our spacecraft structure (a ductless blunt body with a circular cross-section) [6]. The authors related the drag coefficient of these re-entry vehicles to mach numbers for hypersonic flow. From this paper, we determined that a coefficient of drag of 1.4 was appropriate for our application. Then using this value in conjunction with the mass and aerodynamic area, we determined that the ballistic coefficient for our mission is 45.7 kg/m^2. This is reasonably close to that of the stardust mission, which was approximately 55 kg/m^2. The lower ballistic coefficient of this mission indicates slightly more oncoming surface area per kilogram of spacecraft.

Contrary to the initial orbital modeling, where pre-capture periapsis heights and conditions at the edge of Earth's sphere of influence were used to specify each unique trajectory, in AMAT one must specify the initial altitude, velocity, and flight-path angle for the equivalent trajectory. Based on where AMAT's data for atmospheric conditions begins, we specify the starting height to be 125 km. Based on our initial trajectory modeling, this corresponds to an initial velocity of 12.39 km/s, regardless of the initial flight-path angle. We chose three flight-path angles to examine our design's performance at trajectories representative of a wide range of conditions. We examined an angle of -90°, which corresponds to re-entering while aimed directly at the center of the earth and is the most aggressive re-entry trajectory possible. An initial flight-path angle of -6°, corresponding to the initial periapsis at 36.3 kilometers above mean sea level, and is about as shallow of an entry as possible with AMAT while still capturing on the first past through the atmosphere.

3

Interestingly, our initial modeling in MATLAB indicated than an angle as low as -5.3° is possible for capturing on the first pass, but with the more accurate atmospheric modeling in AMAT, only initial flight-path angles steeper than -6° captured on the first pass. Finally, an initial flight-path angle of -10.96°, corresponding to an initial periapsis at 100 kilometers below mean sea level, was chosen as representative of trajectories that are neither aggressively steep nor shallow enough to just barely capture on the first pass. We set the propagation time of the AMAT solver to 30 minutes for the purposes of running the simulation. In practice, all the simulations which captured on the first pass finished re-entry in under approximately 10 minutes and were halted when the capsule reached sea-level.

2. Analysis Results

Using the input conditions discussed above, the full re-entry profiles for the three cases were determined in AMAT. Plots of the velocity, deceleration, stagnation point heat rate, and total stagnation point heat load with respect to time for the -10.96°, -90°, and -6° cases are shown in Figures 3, 4, and 5, respectively. In the -10.96° case, we find that the capsule experiences significant g-loading of 56 g's, relatively high maximum stagnation point heat loads of 881 W/cm^2, and a moderate total heat load of 15.4 kJ/cm^2. For the -90° case, the resulting plots look very similar at first glance to the previous case, just scaled up by around an order of magnitude. The deceleration peaks at 400 g's and the maximum stagnation heat flux is 2870 W/cm^2, but interestingly the total heat rate is a measly 7.4 kJ/cm^2. Finally, the -6° case shows a significantly different overall shape in the re-entry profile relative to the other two trajectories. The main deceleration comes in two phases, is spread out over more than 400 seconds, and peaks at just under 8 g's—nearly low enough for a crewed re-entry. Note that an actual crewed re-entry would use a vehicle with a non-zero lift-to-drag ratio to prolong re-entry even longer, but as MSR is uncrewed, a significantly higher g-load is permitted. As expected, the maximum stagnation point heat flux is much lower at under 400 W/cm^2, but very interestingly, the total heat load in this case is significantly higher than either of the two cases.
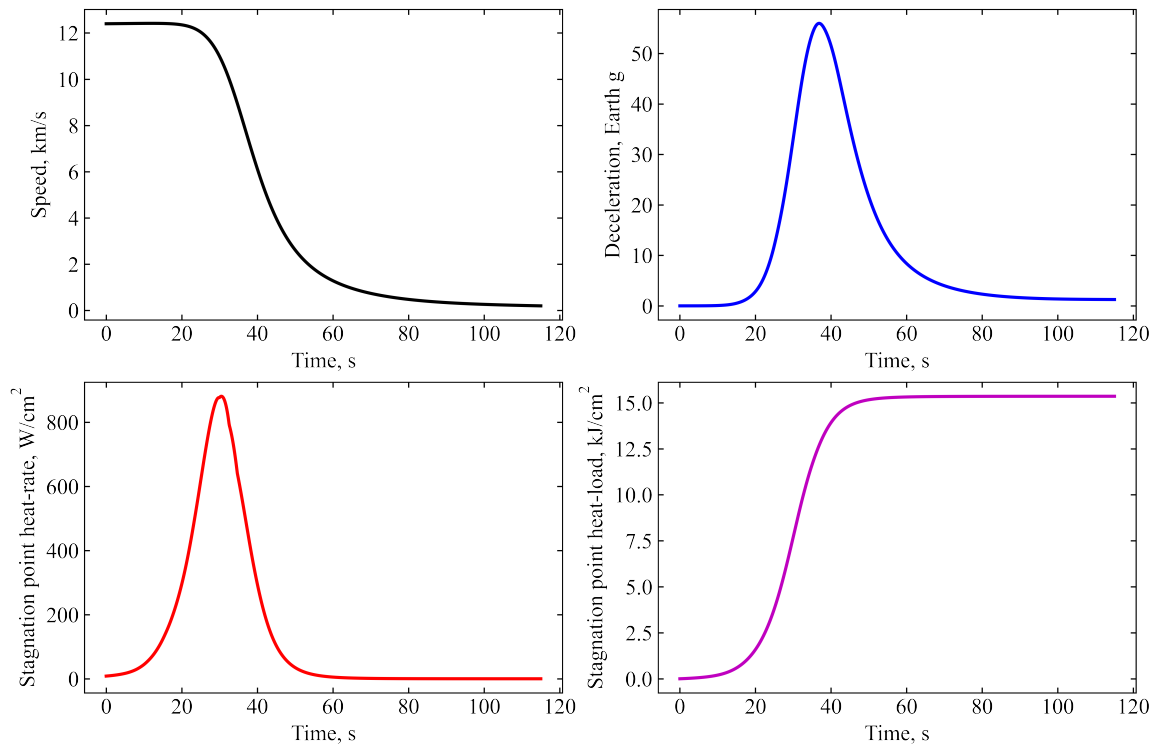

Fig. 3   The time variation of the AMAT results for the $\gamma_0 = -10.96°$ case.

We believe that the total heat load increases with increasing length of re-entry because when the process is very quick (i.e. faster than the heat can penetrate into the heat shield), only the outermost layers of the heat shield have time to heat up. Thus, despite the large amount of heat dumped into the heat shield, past a certain point it cannot increase the surface temperature as it will approach the free-stream temperature. For the slower re-entry trajectories, the rest of the

4

heat shield has time to heat up and increase the effective thermal capacity of the heat shield, thus increasing the total heat load. It should be noted that since all three cases began with the same velocity at the same altitude, they all began with the same amount of energy to be dissipated. The higher heat loads simply indicate that a larger proportion of that energy is absorbed by the re-entry vehicle, as opposed to remaining as heat in the plasma trail behind the vehicle.
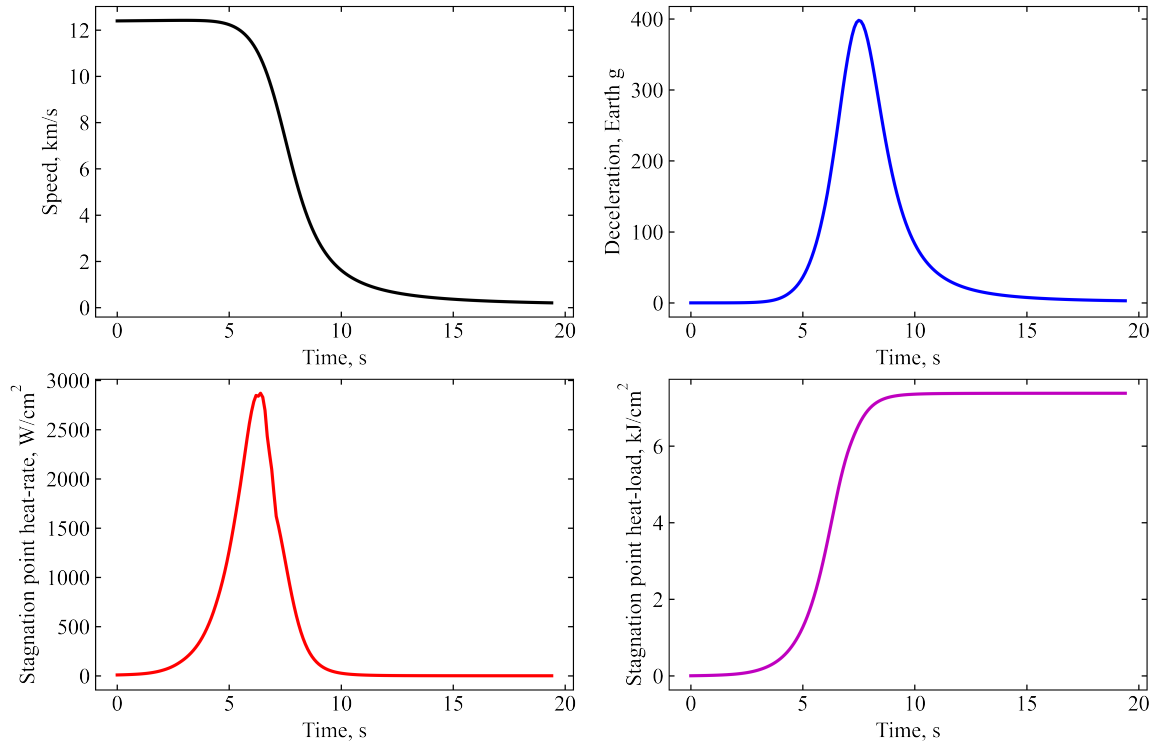

Fig. 4   The time variation of the AMAT results for the $\gamma_0 = -90°$ case.

For the material response analysis, all three conditions were investigated. The -90° case is likely exceeding the structural limits allowable for the heat shield, but this will simply be considered in the final heat shield and trajectory choice in Section V. The boundary conditions found by AMAT were converted into convection coefficients, post-shock enthalpies, and post-shock densities with a script made by Jérémie Meurisse, as these are the boundary conditions required for the PATO material response simulations.

IV. Material Response Analysis

The heat shield material investigated for this study was Theoretical Ablative Composite for Open Testing (TACOT), which is a low-density carbon/phenolic ablator. TACOT is made of 10% carbon fiber, 10% phenolic resin, and 80% porous; its composition is comparable to NASA's Phenolic Impregnated Carbon Ablator [7]. Material response simulations were conducted using PATO, a volume-averaged ablation physics solver. While the software is capable of solving three-dimensional geometries, only one-dimensional cases were investigated for this study to reduce computation cost and due to a lack of full boundary condition resolution in AMAT.

A. Material Response Setup

The computational domain of the material response simulation was set as follows: 1.27 cm of aluminum honeycomb substrate, 0.14 cm of epoxy bonding, and a varied amount of ablator. Two cases of ablator thickness were investigated: 3 cm and 5 cm. Four thermocouples were placed inside the TACOT heat shield at the center, with varied vertical placements described in Table 1. These positions were selected in order to provide comparable results from the two thickness-case-studies.
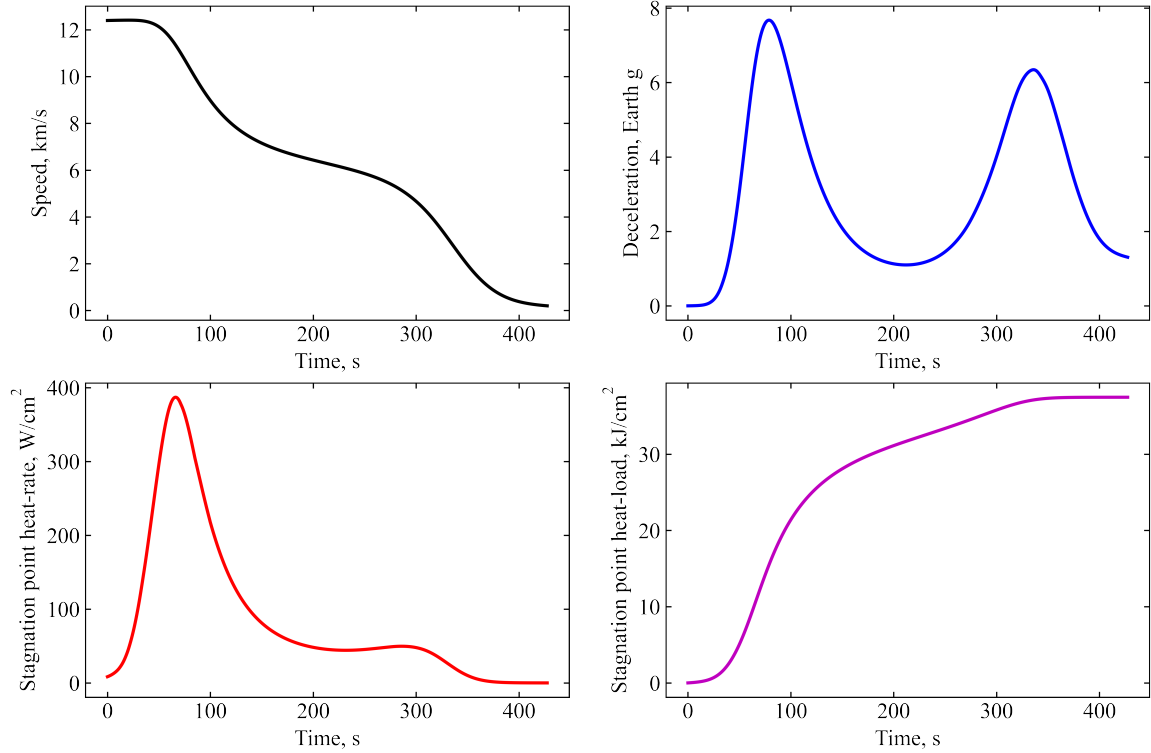
Fig. 5   The time variation of the AMAT results for the $\gamma_0 = -6°$ case.

Table 1   Thermocouples' vertical placement within the center of the heat shield (TC = Thermocouple)

Sensor name	Distance from bondline (cm)
TC1	2.5
TC2	2.0
TC3	1.5
TC4	1.0

B. Material Response Results

6 simulations were completed in PATO, resulting in temperature (wall, bondline, and thermocouples) and recession plots. The calculations for the $\gamma_0 = -90°$ & $t_s = 5$ cm were not able to converge, and failed due to the extremity of the case at the 5th iteration, out of the conventional 133th, which was used in most cases. Hence, the results for that case are not included in this paper. In Figure 6)&7)a)i. & b)i. the end-time was increased to 250 seconds to allow for the convergence of the temperature curves to a steady state value.

1. Temperature

Temperature of the wall, thermocouples, and bondline were plotted over time for the two different thicknesses investigated among different flight-path angles (Figure 6). The wall temperatures across the two different thicknesses for the same flight-path angle were indistinguishable. In the 3 cm thick TACOT case, thermocouples were in the range of 500-2000 K. However, in the 5 cm thick TACOT case, the temperatures of the thermocouples stayed below 800 K, as expected, since the thermocouples are further from the wall compared to the thinner case. Additionally, it is interesting to note that in case Figure 6)a)iii., TC1 starts to burn up at ~ 8 seconds, as its curve aligns with the wall temperature.

The highest bondline temperature experienced was for case a)i., and the lowest was b)ii. (Table 2). This was expected, since the heat shield is skimming the atmosphere at a moderate condition with a thicker material.
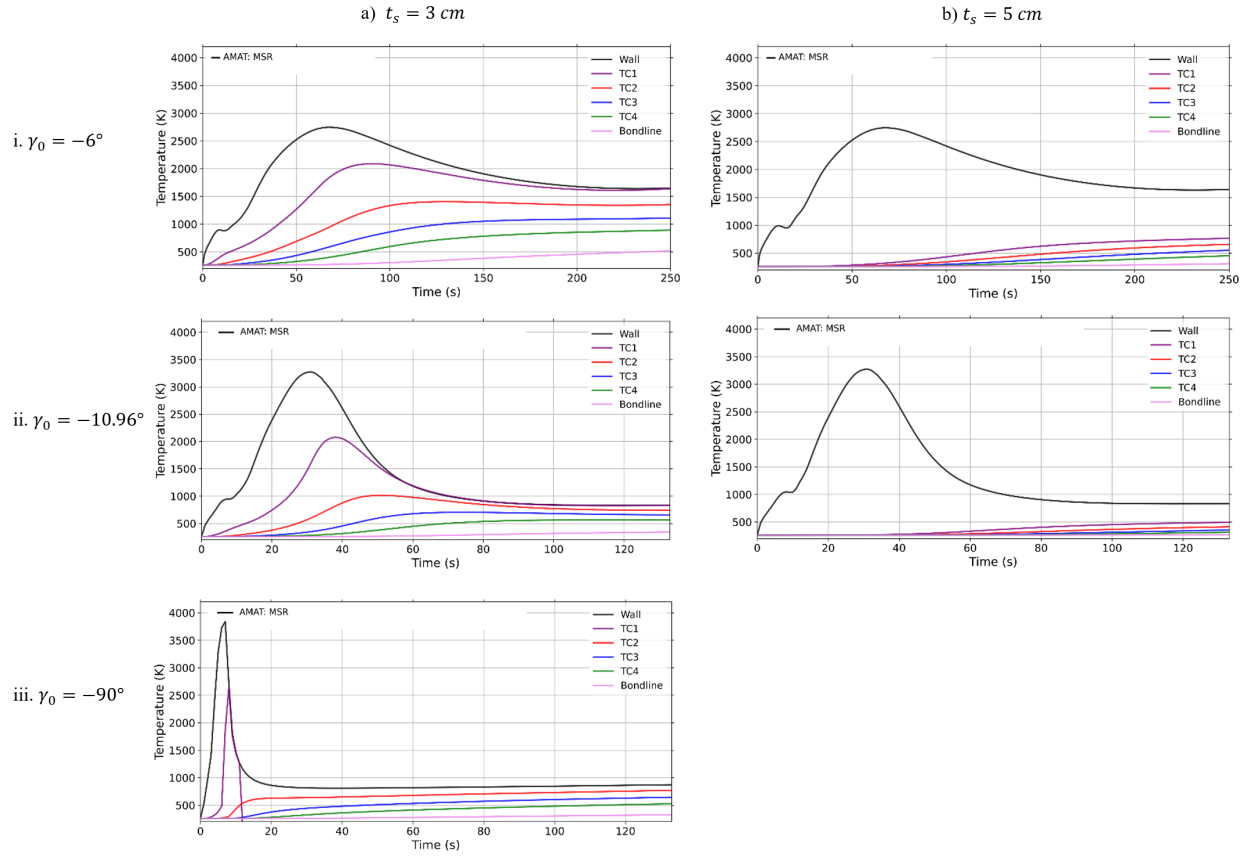
6

Fig. 6   Temperature results of PATO within the thickness & flight-path angle case studies

Table 2   Bondline temperature within the thickness & flight-path angle case studies

T_b (K)		t_s (cm)	
		3 cm	5 cm
γ_0	-6°	516.806	310.875
	-10.96°	344.366	268.185
	-90°	326.927	N/A

2. Recession

Recession was plotted to observe the amount of the TACOT material recessed during the atmospheric entry in PATO (Figure 7). Thickness had negligible effect on the amount of recession experienced by the heat shield. The maximum recession occurred for case 7)a)iii., where the spacecraft is performing a nose-dive toward the center of Earth.

V. Conclusion and Final Selection of Heat Shield Parameters

Based on the results from the simulations, it was determined γ_0= -10.96°performed better than γ_0= -6°& -90°, since it showed promising temperatures at lower steady state values by 500K, and faster entry time resulting in lower heat-load values. Very similar recession results ($\sim$ 5 mm) for most of the cases, except for 90°with t_s = 3 cm which had a recession value of $\sim$ 7 mm. It was also concluded that for a steeper flight-path angle during they entry, expected behavior is: higher maximum deceleration, higher heat-rate during, lower total heat-load, as well as higher risks of mechanical failure, higher peak temperature at stagnation point. Additionally, the results showed that the greater the Thermal Protection System's thickness, the lower the bondline temperatures, and the lower the heat-load is. The trade
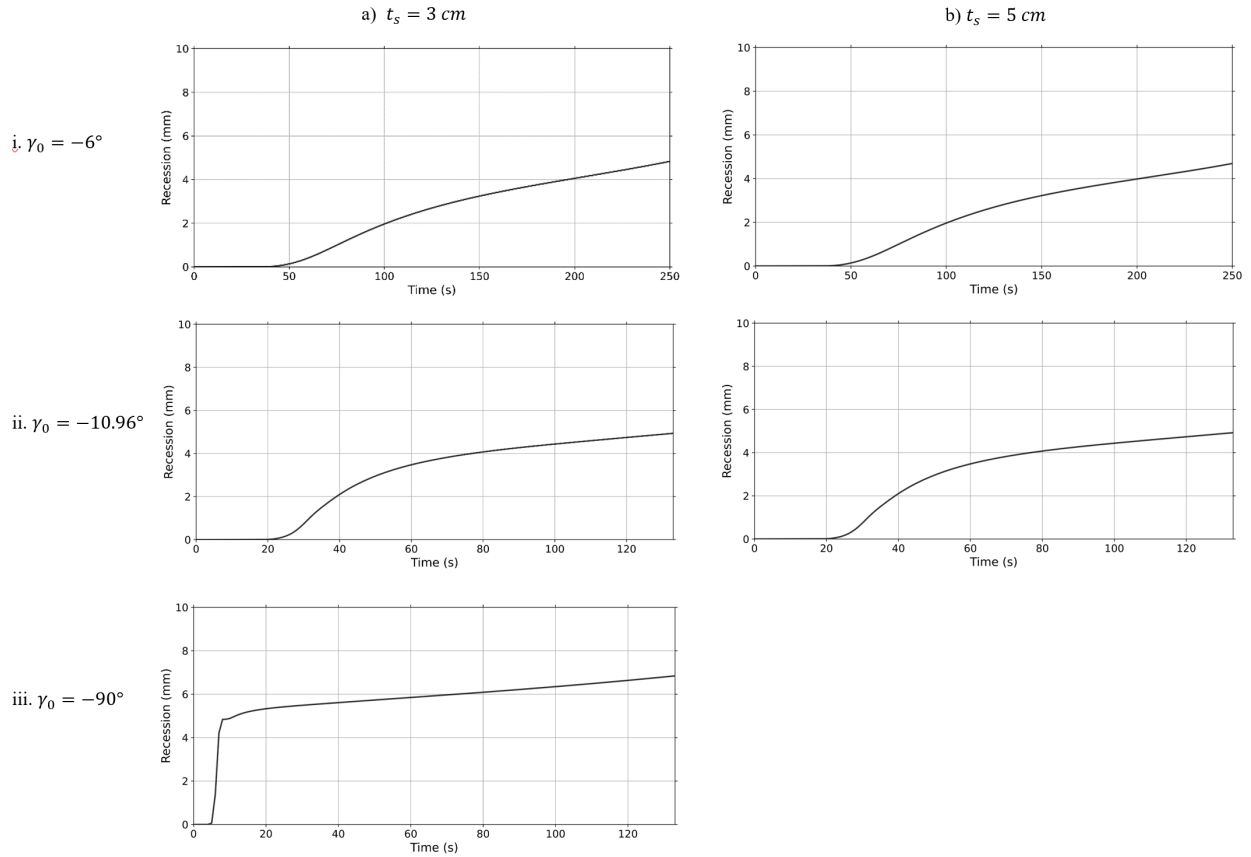
Fig. 7   Recession results of PATO within the thickness & flight-path angle case studies

off is the addition of mass, which was ~ 1.5 kg/cm of thickness for the design of the 5 cm thick TACOT, compared to the 3 cm case.

VI. Future Work

We propose an investigation of different geometries/topologies of the TACOT material, in addition to implementing new materials in the analysis. Additionally, more extreme thickness cases might show promising trends that were not observed in this study. Porous Microstructure Analysis (PuMA) can also be utilized to analyze artificial porous structures.

Acknowledgments

References

[1] NASA, "Concepts for Mars Sample Return," Available at `https://mars.nasa.gov/mars-exploration/missions/mars-sample-return/` (2020/02/26), 2020.

[2] Price, C., "Mars Sample Return Spacecraft Systems Architecture," 2000. https://doi.org/10.1109/AERO.2000.879302.

[3] Anderson, J. D., *Hypersonic and High Temperature Gas Dynamics*, 1st ed., McGraw-Hill, New York, 1989.

[4] Gupta, R. N., "Aerothermodynamic Analysis of Stardust Sample Return Capsule with Coupled Radiation and Ablation," *Journal of Spacecraft and Rockets*, Vol. 37, No. 4, 2000, pp. 507–514.

[5] Park, C., "Calculation of Stagnation-Point Heating Rates Associated with Stardust Vehicle," *Journal of Spacecraft and Rockets*, Vol. 44, No. 1, 2007, pp. 24–32.

[6] Anbu, C., Raj, S., Narasimharavadhan, M., Vaishnavi, N., Aruvinthan, S., Arjani, A. A., and Pillai, S. N., "Aerodynamics of ducted re-entry vehicles," *Chinese Journal of Aeronautics*, Vol. 33, 2020, pp. 1837–1849. https://doi.org/10.1016/j.cja.2020.02.019.

[7] Lachaud, J., van Eekelen, T., Scoggins, J. B., Magin, T. E., and Mansour, N. N., "Detailed chemical equilibrium model for porous ablative materials," *International Journal of Heat and Mass Transfer*, Vol. 90, 2015, pp. 1034–1045.